



Acoustic performance optimization of a cementitious composite with a porous medium

Sen Lin^{a,c}, Genbao Zhang^{b,*}, Junbo Sun^d, Shilin He^e, Changfu Chen^e, Amr M. Morsy^{f,g}, Xiangyu Wang^d

^a State Key Laboratory of Advanced Design and Manufacturing for Vehicle Body, College of Mechanical and Vehicle Engineering, Hunan University, Changsha, Hunan, 410082, PR China

^b College of Civil Engineering, Hunan City University, Yiyang, Hunan, 413000, China

^c Guangxi Key Laboratory of Disaster Prevention and Engineering Safety, Guangxi University, Nanning, Guangxi, 530004, PR China

^d Australasian Joint Research Centre for Building Information Modelling, Curtin University, Perth, 6102, Australia

^e Key Laboratory of Building Safety and Energy Efficiency of the Ministry of Education, College of Civil Engineering, Hunan University, Changsha, Hunan, 410082, PR China

^f School of Architecture, Building and Civil Engineering, Loughborough University, Leicestershire, LE11 3TU, United Kingdom

^g Department of Civil Engineering, Cairo University, Giza, 12613, Egypt

ARTICLE INFO

Keywords:

Cementitious composite
Sound absorption
Topology optimization
Bidirectional evolutionary structural optimization (BESO)

ABSTRACT

This paper presents an optimization algorithm for band-gap maximization aimed at designing the porosity of a cementitious composite. Numerical analysis revealed the relationship between the composite porosity and band structure. With the utilization of gravels as the main aggregate, microbeads and a vesicant were also mixed to produce the porous cementitious composite, where correlative experiments were conducted on the mixture proportion. Digital microscope images were applied to evaluate the micro-construction details of the composite. The acoustic performance of the porous concrete was tested by an impedance tube. The results show that the maximum sound absorption coefficient of the phononic crystal composed of 4 mm gravels and surrounding microbeads can reach 90%. The frequency corresponding to the peak value is 1490 Hz, which is consistent with the frequency range of the band gap from theoretical derivation and simulation analysis. This developed methodology is expected to be applied to the design of cementitious structures to achieve sound absorption performance enhancement.

1. Introduction

Sound-absorbing structures, which are typically developed using a combination of low- and high-index materials, are periodic structures designed to affect the motion of acoustic waves by impeding the propagation of waves in particular directions within certain frequency ranges known as band gaps. As an analogue of sound-absorbing structures, phononic crystals have been widely studied over the past decade [1]. In their micro-scale applications, phononic crystals offer rigid attachments for vibrating devices with their substrates, such as gyroscopes, bionic structures [2], and mechanical resonators [3].

There are various methods for the calculation and optimization of the band structures of phononic crystals. Sigmund and Jensen [4] applied the finite-element method (FEM) and the method of moving

asymptotes (MMA) to maximize the band gaps of phononic crystals. Nevertheless, optimization can only start from the initial design with existing band gaps. The FEM was extensively used to compute the band structures of three-dimensional phononic crystals from a geometrical perspective, and was verified by calculating the band structures of three-dimensional locally resonant phononic crystals [5]. Alternatively, the finite-difference time-domain (FDTD) method was developed incorporating with a performance computing (PC) cluster system to process and accelerate the calculation of the band gap phenomena of 3D phononic crystals [6]. To realize novel phononic crystal designs, Gazonas et al. [7] proposed a genetic algorithm (GA) associated with the FEM to optimize a 2D phononic crystal with a hexagonal lattice for acoustic waves. Additionally, a GA was also combined with the fast plane wave expansion (FPWE) method to optimize 2D phononic band gap crystals [8]. However, the low efficiency of GAs is inadequate for

* Corresponding author.

E-mail addresses: senlin@hnu.edu.cn (S. Lin), genbao@hncu.edu.cn (G. Zhang), tunneltc@gmail.com (J. Sun), 943873352@qq.com (S. He), cfchen@hnu.edu.cn (C. Chen), a.morsy@lboro.ac.uk (A.M. Morsy), xiangyu.wang@curtin.edu.au (X. Wang).

<https://doi.org/10.1016/j.job.2021.103362>

Received 27 April 2021; Received in revised form 9 September 2021; Accepted 21 September 2021

Available online 23 September 2021

2352-7102/© 2021 Elsevier Ltd. All rights reserved.

Notations	
<i>Basic SI units are given in parentheses</i>	
ρ_1	the density of gravel (kg/m ³)
λ_1, μ_1	Lamé constants of gravel (GPa)
ρ_2	the density of porous medium (kg/m ³)
λ_2, μ_2	Lamé constants of porous medium (GPa)
a	the size of discretized square element of composite structure
$\mathbf{u}_{(r,k)}$	the displacement vector of point of interest
t	the time
∇	the gradient operator
x, y, z	the cartesian coordinates of point of interest
\mathbf{r}	the position vector of point of interest
$\mathbf{u}_{(r)}$	the periodic function of \mathbf{r}
\mathbf{k}	the Bloch wave vector of point of interest
k_x, k_y, k_z	the components of \mathbf{k} of point of interest
ω	the angular frequency of the elastic medium
n_p	the number of periods
U	the vector of displacements at all the element nodes
K	the stiffness matrix of the whole discrete system
M	the mass matrix of the whole discrete system
x_e	the design variable characterizing element material composition
$f(x_e)$	the normalized band gap size
V	the volume fraction of solid composing of the element
δ	the limit of solid volume fraction ensuring concrete manufacturability
$\omega_n(\mathbf{k})$	the n th eigenfrequency of the element
$\mathbf{u}(\mathbf{k})_n$	the normalized eigenvector
N_p	the total number of points along the Brillouin zone
p	the parameter characterizing the type of P-norm
C_{p1}	the upper bound of the minimum eigenfrequency
C_{p2}	the lower bound of the maximum eigenfrequency
α_e	the sensitivity number for frequency maximization
$\hat{\alpha}_i$	the filter converting sensitivity number from element to node
r_{ei}	the distance between the center of element e and node i
$w(r_{ei})$	the weight factor in defining α_e
r_{\min}	the prescribed filter radius in defining $w(r_{ei})$
l	the current iteration number
$\Phi(o)$	the LSF value at an arbitrary point within the design domain
N_o	the counter of element
o	an arbitrary point located in element N_o
$\zeta_o, \eta_o,$ and γ_o	the corresponding natural coordinates of the considered point
$(\alpha_i)^{N_o}$	the i th node sensitivity number of element N_o
$\zeta_{ib}, \eta_{ib},$ and γ_i	the coordinates of $(\alpha_i)^{N_o}$
S	the level-set value
D	the design domain in setting S
Ω	the cement regions in setting S
T	the boundaries setting S
V^*	the prescribed volume in evolution
ER	the evolution rate
Φ_i^l	the LSF values at all nodes of element i
N_{ap}	the number of points in element grid
N_{lp}	the number of points whose LSF value exceeds S
τ	the convergence error in iterations
q	the lower iteration number for convergence check
Q	the upper iteration number for convergence check
C_t	the transverse wave speed
u_p	the displacement in formulation of wave propagation
σ_{pq}	the stress in formulation of wave propagation
ϵ_{rs}	the strain in formulation of wave propagation
C_{pqrs}	the stiffness tensor in formulation of wave propagation

optimization involving numerous computations, such as those of 3D structures. Consequently, an efficient optimization algorithm should be selected for the design of 3D phononic crystals. Well-established optimization algorithms include solid isotropic material with penalization (SIMP) [9,10], level set [11], and bidirectional evolutionary structural optimization (BESO) [12,13]. BESO applies discrete design variables so that the resulting optimized structure has a clear but zig-zag boundary. An improved BESO algorithm, named evolutionary topology optimization (ETO), has recently been proposed [14], which enables the determination of a smooth structural topology boundary with a constructed level-set function (LSF).

A phononic crystal slab, namely, a slab with a periodic variation in material constants in the plane, has been experimentally studied by Zhang et al. [15], who identified directional band gaps for slab or plate modes for surface acoustic waves. However, Khelif et al. [16] claimed that surface acoustic waves could only occur in semi-infinite media, or at least in slabs much thicker than the surface wave penetration depth. For two-dimensional phononic crystal slabs, the frequency band gap width and frequency range have been experimentally measured [17,18]. Nevertheless, phononic crystals are assumed to be infinitely thick or extremely thin in theoretical analysis [15], whereas actual models in experiments exhibit a finite size and thickness [16,17]. Selecting the slab with the simplest geometry as an example, the corresponding band structures and band gaps can greatly differ as the thickness varies. Sainidou et al. [19] evaluated the band gaps in three-dimensional binary systems composed of steel spheres in polyester, and revealed the impact of the geometry of the structure on the width of the band gaps. It is noteworthy that a three-component system is characterized by the adjustability of wave gap, e.g. the wave gap of this system can be

continuously tuned from a resonance gap to a Bragg gap by adjusting the softness of the coating [20].

For civil engineering applications based on the concept of phononic crystals, concrete is a dense material that is capable of reflecting sound waves (i.e., the sound absorption is insignificant). Nevertheless, the wave absorption performance of cement-based materials can be improved by changing the material composition and construction [21]. Cement with specific additive materials can create composites with distinguished wave absorbing capability, which have received research interest in civil engineering [22]. In non-porous cement-based composites, the solid–solid interfaces could enhance the sound absorption capability because sound waves are refracted and reflected at the interface [23]. A road sound barrier composed of coal/fired slag and cement was developed and analysed to examine the influence of slab thickness and particle size distribution on sound absorption [24]. The sound absorption capability of expansive clays was reported to depend on the particle size and the acoustic flow resistance [25]. Use of waste concrete as an aggregate in preparing porous concrete sound-absorbing plates can reach an optimal porosity of 25% [26]. The sound absorption capability of concrete specimens can be doubled by adding a 40% by volume of hollow microbeads consisting of aluminium silicate [27]. In addition, when preparing porous concrete, the surface area of pores can be increased by using a foaming agent, which improves sound absorption performance [28].

While several studies were carried out to research the effect of porosity on concrete sound absorption, the literature lacks a theoretical derivation or optimization design of porosity parameters. In this paper, an optimization algorithm for band-gap maximization is presented for the selection of target porosity in cementitious composite mix designs.

Numerical analysis facilitated the development of a relationship between the composite porosity and band structure. In addition, correlative experiments were conducted on mixtures with various ingredient proportions. With the use of gravel as the main aggregate, microbeads and vesicants were also added to produce porous cementitious composite mixtures. Further, digital microscope images were observed to evaluate the micro-construction details of the composite mixtures. The acoustic performance of the porous concrete was tested by an impedance tube. The results show that the phonic crystal composed of gravels and surrounding microbeads have significant sound absorption performance, which is in good agreement with numerical predictions. The proposed methodology is applicable to design of cementitious structures to enhance their sound absorption capability.

2. Analysis of porous cementitious sound-absorbing slab

The fabrication procedure and simplified geometry of the cementitious composite are depicted in Fig. 1(a). Porous cementitious sound-absorbing slabs are a novel type of cement matrix composite consisting of gravel as aggregate, cement as gel, water, and additives. Gravel particles of different sizes and shapes were coated with a thin layer of cement slurry as the cement layer. These aggregate particles are bonded to each other and form an internal pore network resulting in homogeneous porous structures. Open microbeads are saturated with water before hydration and dispersed throughout the aggregate particles. After the concrete particles have been produced, the microbeads lose their internal water and form cavities (i.e., pores) around the aggregate particles. During acoustic wave propagation, the air entrapped within the pores vibrates and rubs against solid surfaces [29]. Due to viscosity and thermal conduction effects, acoustic energy is constantly converted into heat energy and is consumed. In this case, the amplitudes of sound waves are attenuated and the sound pressure level decreases, thus achieving the sound absorption effect.

The structure is assumed to be infinite and periodically arranged in the X and Y directions (X and Y directions are parallel to the structure), while it exhibits a finite size in the Z direction (Z direction is normal to the structure). The entire domain initially consists of gravel (density, $\rho_1 = 1850 \text{ kg/m}^3$; Lamé constants, $\lambda_1 = 16.67 \text{ GPa}$ and $\mu_1 = 25.1 \text{ GPa}$) embedded in a porous medium consisted by cement and microbeads (density, $\rho_2 = 1200 \text{ kg/m}^3$; Lamé constants, $\lambda_2 = 0.76 \text{ GPa}$ and $\mu_2 = 1.61 \text{ GPa}$). The entire plate is discretized to periodic cubic elements with the dimension a (shown in Fig. 1), where the radius of the gravel depends on the porosity of the composite. The governing equation for the heterogeneous elastic medium can be expressed as follows:

$$\rho(\mathbf{r}) \frac{\partial^2 \mathbf{u}(\mathbf{r}, \mathbf{k})}{\partial t^2} = \nabla \{ [\lambda(\mathbf{r}) + 2\mu(\mathbf{r})] (\nabla \cdot \mathbf{u}(\mathbf{r}, \mathbf{k})) \} - \nabla \times [\mu(\mathbf{r}) \nabla \times \mathbf{u}(\mathbf{r}, \mathbf{k})] \quad (1)$$

where λ and μ are Lamé constants; ρ is the mass density; $\mathbf{u}(\mathbf{r}, \mathbf{k})$ is the displacement vector; t is the time, ∇ is the gradient operator, and $\mathbf{r} = (\cdot, y, z)$ is the position vector [30]. According to the Bloch's theorem, the displacement vector can be expressed as follows:

$$\mathbf{u}(\mathbf{r}, \mathbf{k}) = \mathbf{u}(\mathbf{r}) e^{i(\mathbf{k} \cdot \mathbf{r})} e^{i\omega t} \quad (2)$$

where $\mathbf{u}(\mathbf{r})$ is a periodic function of \mathbf{r} with the same periodicity as the structure, $i = \sqrt{-1}$, $\mathbf{k} = (k_x, k_y, k_z)$ is the Bloch wave vector, and $\omega = 2\pi n_p$ is the angular frequency. By solving the above equations with the FEM, the generalized eigen value equation in discrete form can be written as follows:

$$(K(\mathbf{k}) - \omega^2 M) U = 0 \quad (3)$$

where U is the column vector formed by the displacements at all the element nodes in the calculation area, and K and M are the stiffness and mass matrices, respectively, of the whole discrete system. The detailed derivation of K and M is provided in the Appendix.

A gravel/porous medium system with a specific filling fraction was chosen for the investigation due to the clear complete band gap for bulk wave propagation in the plane of an infinite structure. The band structure along the high-symmetry axis of the first Brillouin zone [31], i.e., along the $\Gamma_b(0,0)$ - $X_b(\pi/a,0)$ - $M_b(\pi/a,\pi/a)$ - $\Gamma_b(0,0)$ path, was considered in this study.

Selecting the band structure of the cementitious composite of size $a = 8 \text{ mm}$ and gravel volume fraction $V = 0.6$ (the shape is square) as an example, the unit cell is discretized into $16 \times 16 \times 16$ linear eight-node brick elements. The band diagram is calculated by using the plane wave expansion (PWE) method, and the corresponding result is shown in Fig. 2. This figure clearly shows the variation in eigen frequencies along the boundaries of the first irreducible Brillouin zone. A complete elastic band gap (the 2nd band) is visibly observed in the mid-frequency region (920–930 Hz), which was used in the subsequent optimization (see Fig. 3).

3. Topology optimization

The entire BESO optimization procedure is outlined in the above flow chart. The optimization objective in this paper is to maximize the band gap between consecutive frequency modes of the composite. To characterize this objective by accommodating with different eigen values, the normalized band gap size $f(x_e)$ corresponding to the relative gap ratio was used as the objective function, written as follows:

$$\begin{aligned} \text{Max} : f(x_e) &= 2 \left[\frac{\min \omega_{n+1}(\mathbf{k}) - \max \omega_n(\mathbf{k})}{\min \omega_{n+1}(\mathbf{k}) + \max \omega_n(\mathbf{k})} \right] \\ \text{st} : V &\geq \delta \end{aligned} \quad (4)$$

where x_e is the design variable characterizing the material composition of an element; $\omega_n(\mathbf{k})$ and $\omega_{n+1}(\mathbf{k})$ represent the n th and $(n+1)$ th eigen values of the element respectively; V denotes the volume fraction of the solid (i.e. the cement and the aggregate) composing of the element; δ denotes the lower limit of solid volume fraction ensuring the concrete manufacturability.

According to previous research on phononic crystals, the band gap width is generally determined by the property contrast of composites [32]. Accordingly, a linear material interpolation scheme was deployed herein as follows:

$$\begin{cases} \rho(x_e) = (1 - x_e)\rho_1 + x_e\rho_2 \\ \lambda(x_e) = (1 - x_e)\lambda_1 + x_e\lambda_2 \\ \mu(x_e) = (1 - x_e)\mu_1 + x_e\mu_2 \end{cases} \quad (5)$$

where the subscripts denote the two materials composing of the element. The element is wholly composed of material 1 when $x_e = 0$, and is wholly composed of material 2 when $x_e = 1$. Due to the sensitivity of variable variation, the change in x_e was limited to 0.1 between each iteration, and x_e was varied from 0 to 1. Moreover, the value naturally approaches 0 or 1 at the end of the optimization process. Note that the value of x_e can only be defined as either 0 or 1 in the traditional BESO process [33].

Afterwards, the sensitivity of the objective function, f , with respect to design variable x_e can be written as follows:

$$\frac{df(x_e)}{dx_e} = 4 \frac{\max \omega_n(\mathbf{k}) \frac{\partial \min \omega_{n+1}(\mathbf{k})}{\partial x_e}}{(\min \omega_{n+1}(\mathbf{k}) + \max \omega_n(\mathbf{k}))^2} - 4 \frac{\min \omega_{n+1}(\mathbf{k}) \frac{\partial \max \omega_n(\mathbf{k})}{\partial x_e}}{(\min \omega_{n+1}(\mathbf{k}) + \max \omega_n(\mathbf{k}))^2} \quad (6)$$

Additionally, the element sensitivities of the eigen frequencies can be obtained as follows:

$$\frac{\partial \omega_n(\mathbf{k})}{\partial x_e} = \frac{1}{2\omega_n} \mathbf{u}(\mathbf{k})_n^T \left(\frac{\partial K}{\partial x_e} - \omega_n^2 \frac{\partial M}{\partial x_e} \right) \mathbf{u}(\mathbf{k})_n \quad (7)$$

where $\mathbf{u}(\mathbf{k})_n$ is the eigenvector normalized with respect to the global mass matrix. Additionally, the element sensitivities are obtained by averaging the neighbouring elements on the different layers, which

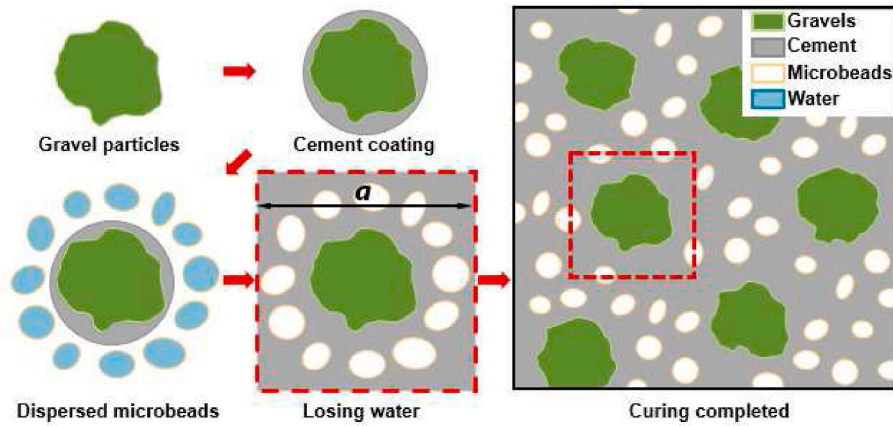


Fig. 1. Principle of the sound absorption capability of the cementitious composite: sketch of the fabrication procedure.

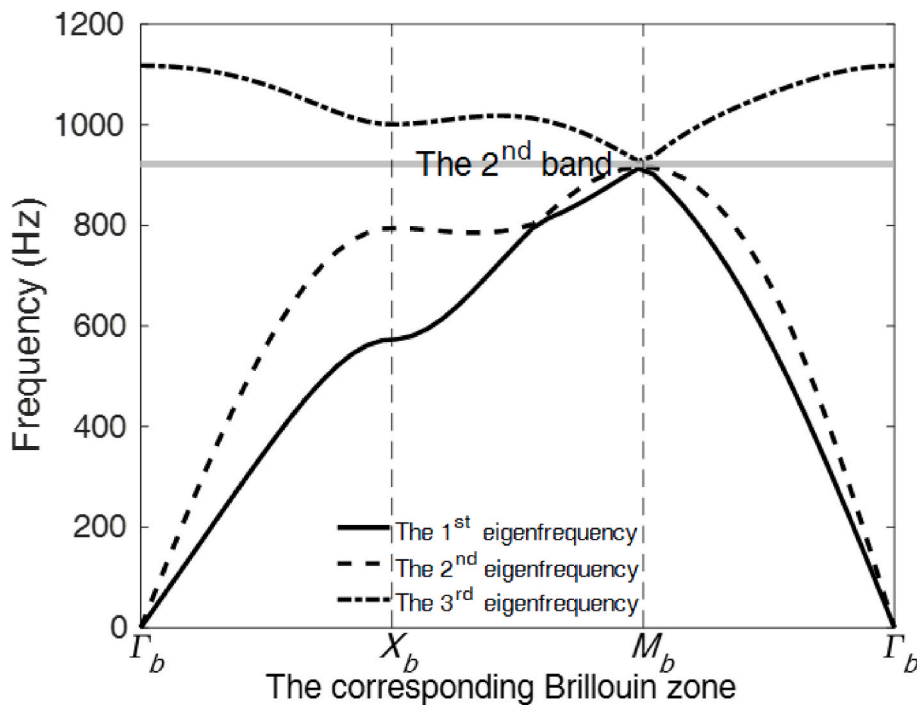


Fig. 2. The 1st-3rd eigenfrequencies and the 2nd band gap of the cementitious composite.

depends on the thickness of the composite. This occurs because the topology optimization is conducted similar to 2D pattern optimization.

To maximize the specified band gap, the optimization process starts from the initial design and gradually redistributes material phases by changing the design variable of each cell. The maximum and minimum values of the objective function are generally not stable during this process. To address this problem, a previous study introduced upper and lower bounds (C_1, C_2) for the corresponding minimum and maximum eigen frequencies, respectively [34]. In this case, all the eigen frequencies between $[\min\omega_{n+1}(\mathbf{k}), C_1]$ for the $(n+1)^{th}$ and above bands, and $[C_2, \max\omega_{n+1}(\mathbf{k})]$ for the n^{th} and below bands are considered for the optimization process. However, it is not precise to set a certain value for C_i (i.e., 0.9 or 1.1), and the corresponding assumptions are difficult to understand. Consequently, this study introduces a P-norm herein rather than C_i .

$$\begin{cases} C_{p1} = \left(\frac{1}{N_p} \sum_1^{N_p} \omega_{n+1}^{1/p}(\mathbf{k}) \right)^p \\ C_{p2} = \left(\frac{1}{N_p} \sum_1^{N_p} \omega_{n+1}^p(\mathbf{k}) \right)^{1/p} \end{cases} \quad (8)$$

where N_p is the total number of points along the Brillouin zone, and p is a positive integer characterizing the type of P-norm, which is set to 8 here. Subsequently, all eigenfrequencies between $[\min\omega_{n+1}(\mathbf{k}), C_{p1}]$ for the $(n+1)^{th}$ and above bands and $[C_{p2}, \max\omega_{n+1}(\mathbf{k})]$ for the n^{th} and below bands are considered for the formulation of the optimization problem.

The sensitivity number for frequency maximization, α_e , can be defined as follows:

$$\alpha_e = \frac{\partial\omega_n(\mathbf{k})}{\partial x_e} \quad (9)$$

Because nodal sensitivity numbers are adopted rather than elemental

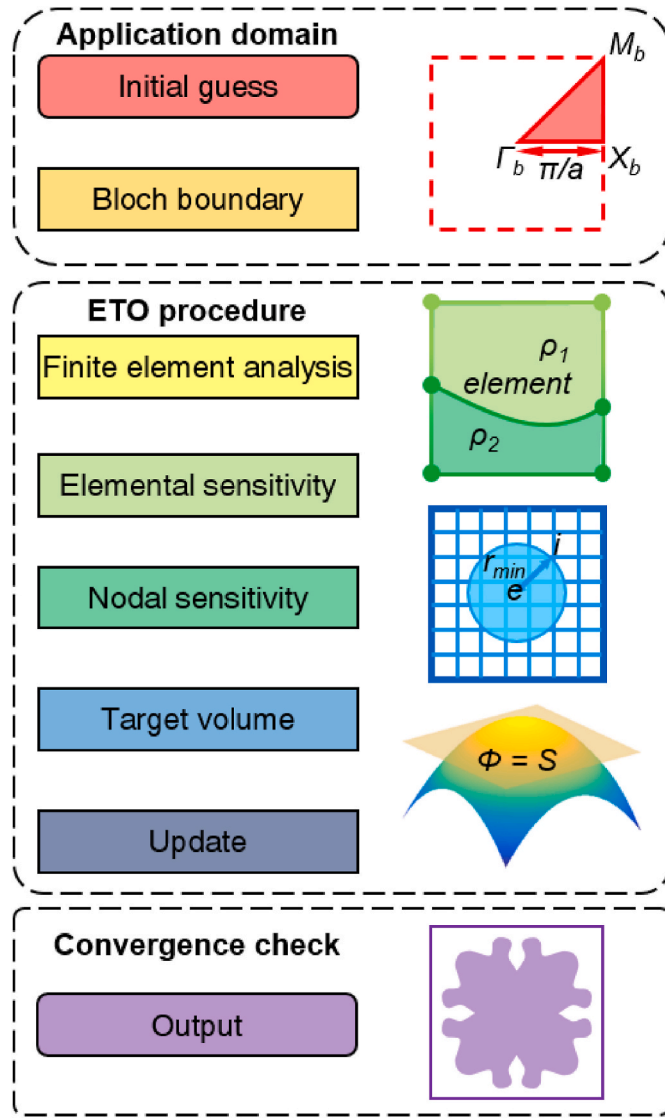


Fig. 3. Flowchart of the BESO optimization procedure.

ones for the evolutionary topology update procedure, the above element sensitivity numbers need to be converted into a nodal expression. To eliminate checker-board patterns and the mesh-dependency, the elemental sensitivity numbers are converted into smoothed nodal sensitivity numbers by a filter $\hat{\alpha}_i$ as defined:

$$\hat{\alpha}_i = \frac{\sum w(r_{ei})\alpha_e}{\sum w(r_{ei})} \quad (10)$$

where r_{ei} is the distance between the centres of element e and node i , and $w(r_{ei})$ is the weight factor given as follows:

$$w(r_{ei}) = \max(0, r_{\min} - r_{ei}) \quad (11)$$

where r_{\min} is the prescribed filter radius. To further improve the convergence of the objective function, f , the nodal sensitivity is modified with its sensitivity history as follows:

$$\hat{\alpha}_i^l = \frac{\hat{\alpha}_i^l + \hat{\alpha}_i^{l-1}}{2} \quad (12)$$

where l is the current iteration number.

During the optimization process, the level-set method is applied for the design of smooth boundaries. For 3D brick elements, the LSF value at

an arbitrary point within the design domain can be expressed using nodal sensitivity numbers as follows:

$$\Phi(o) = \sum_{i=1}^8 \frac{1}{8} [(1 + \zeta_o \zeta_i) + (1 + \eta_o \eta_i) + (1 + \gamma_o \gamma_i)] (\alpha_i)^{N_o} \quad (13)$$

where o is an arbitrary point located in element N_o ; ζ_o , η_o , and γ_o are the corresponding natural coordinates of the considered point; and $(\alpha_i)^{N_o}$ is the i th node sensitivity number of element N_o , whose coordinates are represented as ζ_i , η_i , and γ_i . With the above nodal sensitivity, the level-set method classifies the design domain (D) into cement regions (Ω), air regions (D/Ω), and boundaries (T) by setting the level-set value S , which is updated every iteration as follows:

$$\begin{cases} \Phi(o) > S & (o \in \Omega) \\ \Phi(o) = S & (o \in T) \\ \Phi(o) < S & (o \in D/\Omega) \end{cases} \quad (14)$$

In the evolution process, the program starts from the initial design and gradually reduces the cement volume fraction to a prescribed volume V^* as follows:

$$V^{l+1} = V^l(1 - ER) \quad (V^{l+1} > V^*) \quad (15)$$

where ER is the evolution rate and is set to 2% throughout this study. Due to the complex nature of the solution space, there may be many local optima corresponding to different volume fractions. In this case, the current optimization is limited to determining the optimal solution around the specified volume fraction. Once the volume fraction is below this value, the optimization process enters a metamorphosis stage. The volume fraction is determined by the variation trend of the objective function as follows:

$$V^{l+1} = V^l \left\{ 1 + \frac{|f(x_e^l) - f(x_e^{l-1})| (V^l - V^{l-1})}{|f(x_e^l) - f(x_e^{l-1})| |V^l - V^{l-1}|} ER \right\} \quad (16)$$

According to the function, the target volume fraction in the next iteration is obtained by the variation in the objective function and volume fraction in the last step. A decreasing volume fraction leads to an increase in the objective function $f(x_e)$. Hence, the target volume fraction in the next iteration continues to decrease and vice versa. However, the finite element model based on a fixed grid divides the elements into three groups, i.e., cement, air and boundary elements, as discussed earlier. Consequently, the volume fraction of each element must be calculated as follows:

$$V_i = \begin{cases} 1 & \text{for } \min \Phi_i^l > S \\ 0 & \text{for } \min \Phi_i^l < S \\ N_{lp}/N_{ap} & \text{otherwise} \end{cases} \quad (17)$$

where Φ_i^l are the LSF values at all nodes of element i . For a boundary element, the element can be assumed to be divided into fine grids with N_{ap} points. N_{lp} is the number of points whose LSF value exceeds S . The optimization procedure iteratively updates the topology until the following convergence criterion is satisfied:

$$\frac{|\sum_{q=1}^Q [f(x_e^{l-q+1}) - f(x_e^{l-Q+1})]|}{\sum_{q=1}^Q f(x_e^{l-q+1})} \leq \tau \quad (18)$$

where Q, q are the iteration numbers, Q is set to 5 here. τ is the convergence error, which is set to 0.01%.

4. Numerical results

In this study, a cementitious composite was designed in terms of material and geometrical parameters to achieve the optimized sound absorption capability. The objective is to maximize the 2nd band gap

with solid material constraint, δ . The eigen frequency ω is normalized by $\omega a / 2\pi C_t$, where C_t is the transverse wave speed.

The corresponding band diagram and optimization algorithm were conducted by MATLAB. The optimization history and corresponding topological patterns of the cell whose design domain has an element size of $a = 8$ mm are shown in Fig. 4(a). Furthermore, it is important to consider the effect of element size on the band structure of such square-lattice structure. To evaluate the effect of this single parameter a , the initial design remains the same as that of the square-like solid material at the centre surrounded by air in the following study ($V = 0.90$). The evolution ratio is $ER = 2\%$, and the filter radius is $r_{\min} = a/8$. The solid material constraint, δ , is set to 0.3. However, the volume fraction, V , was justified in each iteration and convergent when the objective function reaches its maximum value, as described earlier. In this study, we simulated different values of element size a and corresponding 2nd band gaps shown in Fig. 4(b).

According to the results, the normalized band gap size $f(x_e)$ experiences a sharp increase from negative (the condition that the maximum value of the lower eigenfrequency is larger than the minimum value of the higher frequency, which likes the first and second eigenfrequency in Fig. 2) to zero values at the beginning of the procedure and subsequently reaches a positive value at a solid volume fraction of $V = 0.69$. Alternatively, a band gap clearly occurs at this stage, and the shape of the solid part changes into a rounded square-like configuration. As expected, V decreases monotonically until it reaches the fluctuation around the constrained value, which results in $f(x_e)$ reaching a maximum value of 9.8% (Fig. 4(a)). Thereafter, the value of $f(x_e)$ fluctuates along with the value of V , and the shape of the solid part continues to change. Finally, the process converges around $f(x_e) = 7.6\%$. Although a lower volume fraction may yield a larger absolute value of the band gap, the objective function $f(x_e)$ still converges at $V = 0.50$, where the band gap reaches its maximum normalized value. Notably, this ideal volume fraction could not be predicted before the optimization procedure. The evolution histories of the band gap size and gravel volume fraction clearly prove the robustness and efficiency of the proposed optimization method.

In terms of the band structure versus the element size a , the minimum value of the 3rd eigen frequency $\min\omega_3 = 1850$ Hz and the maximum value of the 2nd eigen frequency $\max\omega_2 = 1720$ Hz occur at $a = 4$ mm (Fig. 4(b)). With increasing element size, a , the difference of $\min\omega_3$ and $\max\omega_2$ values, namely, the 2nd band gap size, slightly decrease. For instance, if the noise originates from the workstation operation, which lies within the middle of the frequency range (500–1000 Hz), the element size should be larger than 7 mm. In this circumstance, based on the optimum solid volume fraction value $V = 0.50$, the corresponding solid particle dimensions should be larger than 5.6 mm. Notably, the normalized band gap size $f(x_e)$ basically remains constant when the element size varies.

5. Specimen preparation

The specimens were constituted by base material, i.e., Portland cement PO42.5; solid material, i.e., three types of gravel particles (size dimensions of 4, 6, and 8 mm); and porous material, i.e., microbeads. The properties of solid and porous materials are presented in Table 1. Afterwards, the key influencing factors are the presence of microbeads and the size of gravels. The microbeads determined whether phononic crystal cells could be formed, while the size of the gravels affected the frequency at which sound waves are absorbed. In order to intuitively compare the influence of these two factors on the sound absorption performance, six samples with the combinations of two factors and one plain concrete sample were made for comparison. It should be noted that due to the addition of microbeads, the weight of cement and water in the samples also needs to be adjusted accordingly, compare to those did not include microbeads. Additionally, vesicant (2% by mass) was added to each specimen to enhance porous features of the concrete. The mixture

proportions for the various specimens are summarized in Table 2.

According to the standard of sound absorption experiment, the shape and size of specimen section should be consistent with that of impedance tube. In this case, a square section impedance tube with an inner side length of 80 mm was used, thus the section of sample should also an 80 mm side length square. On the other hand, the thickness of the sample depends on the material properties employed [35]. A large thickness (more than 80 mm side length) can eliminate the boundary effect and accurately measure the sound absorption performance of the composite in the ideal state. However, in the process of sample fabrication, gravels would deposit on the bottom of the sample due to gravity, resulting in material heterogeneity. Moreover, for the sample (S7) with large size gravel (8 mm), if the thickness is too small (less than 20 mm), it would be difficult to form uniformly distributed phononic crystals. In this case, the sound absorption performance could not be measured accurately. Therefore, the size of the sound absorbing concrete sample was determined as $80 \times 80 \times 40$ mm. The customized steel mould for the test was composed of side and bottom plates and connecting bolts. The side plates were fixed by bolts and placed atop the bottom plate to form close-grained specimens. To prepare the cementitious composite, cement, gravel and microbeads were proportionally mixed (Table 2) and poured into a mixer for dry mixing. Specifically, the target porosity was the expected pore volume percentage of the total volume of the material in its natural state, which could be reckoned as the pore volume (consisted of microbeads and air pockets generated by vesicant) divide the total volume of the sample. Notably, the materials had different densities. Hence, the masses of the samples were not identical. Afterwards, water and vesicant were stirred in a blender. Finally, the mixed concrete was poured into the mould, and the top surface was levelled. The mould was removed after three days of curing in an environment at a temperature of 21 ± 2 °C and relative humidity of $95 \pm 5\%$. Then, the samples were covered with plastic film and further cured for 25 days.

6. Microstructure observation

To observe the material distribution principle and microstructure of each material sample, all samples were crushed. Subsequently, a 10-mm fragment was selected, and the micro-morphology of the cleavage surface was observed by digital microscope which could show details as small as 4×10^{-4} mm (DVM6, Leica, Germany). As shown in Fig. 5(a), the internal morphology of specimen S1, composed of pure cement, was relatively flat and dense. The two circular pores in the middle were produced by the vesicant, a small amount of which had been dispersed throughout the mixture. This indicates that in the concrete without aggregate particles, the cement hydration degree was relatively high. However, for specimen S2 (Fig. 5(b)), the gravel surfaces (black parts) were smooth, and most of them were oval-like particles. Because of the lack of constraints from sharp edges, the bonding performance between the gravel surfaces and cement was not strong. Although it was not conducive to the concrete strength, it was beneficial for sound absorption performance improvement. Due to the poor cement adhesion to gravel, sound waves caused the gravel particles to vibrate during propagation through the concrete. Therefore, most of the mechanical energy was converted into internal energy. This phenomenon became more prominent after the addition of microbeads (Fig. 5(c)). The microbeads (white parts) distributed around the gravel particles were small particles with irregular shapes, whose internal structure is shown in Fig. 5(d). They exhibited a smooth surface with many cavities inside. This played a crucial role in the microstructure of the sound-absorbing composites. One of their main functions was to further weaken the adhesion between the gravel particles and cement. Another function was to provide more pores, which together with the cement-based material produced a lower-density material consisting of phononic crystals. According to the above calculation, the composites with large gravel particle sizes revealed notable sound absorption effects at low frequencies. However, large gravel particles may result in a high probability of

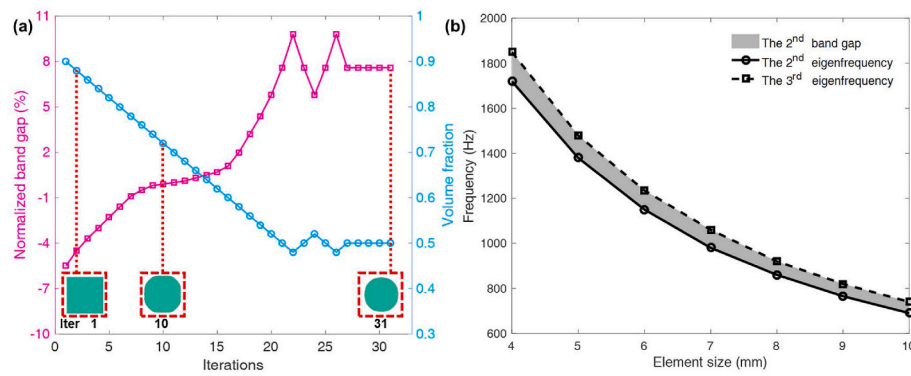


Fig. 4. Band gap optimization of the unit cell. (a) The normalized 2nd band gap size and volume fraction versus the optimization history (note that the initial design and historical topologies are shown at the top). (b) The optimized 2nd band gaps versus element size of a .

Table 1

Material properties of the gravel and microbeads.

Aggregates	Average size (mm)	Bulk density (kg/m ³)	Apparent density (kg/m ³)	1-Hour water absorption (%)	24-Hour water absorption (%)	Porosity (%)
Gravel 1	4.0 ± 0.04	1403 ± 15	1820 ± 19	6.66 ± 0.20	8.26 ± 0.15	0.19 ± 0.005
Gravel 2	6.0 ± 0.07	1420 ± 16	1850 ± 23	6.82 ± 0.12	8.56 ± 0.26	0.20 ± 0.006
Gravel 3	8.0 ± 0.07	1441 ± 13	1860 ± 22	6.85 ± 0.09	8.63 ± 0.14	0.21 ± 0.003
Microbeads	1.0 ± 0.02	180 ± 8	410 ± 18	200 ± 3.2	220 ± 4.0	85 ± 0.2

Table 2

Sound-absorbing cementitious concrete mixture proportions.

Sample ID	Target porosity (%)	Gravel (g)	Gravel size (mm)	Cement (g)	Water (g)	Microbeads (g)	Vesicant (g)
S1	5	–	–	400	200	–	4.0
S2	2	450	4	210	105	–	2.1
S3	50	60	4	280	140	30	2.8
S4	2	450	6	210	105	–	2.1
S5	50	60	6	280	140	30	2.8
S6	2	450	8	210	105	–	2.1
S7	50	60	8	280	140	30	2.8

internal defects. In addition, large gravel particles may sink to the bottom in the process of concrete mixing, which may cause an uneven material distribution in the concrete. Therefore, it is very important to select the appropriate gravel size for the sound absorption performance design of the composites. In order to show the distribution of various substances in different samples, the corresponding digital microscope images are presented in Fig. 5(e–h). As shown in Fig. 5(e), the pores in S1 were different in size (the diameters were 0.2–0.4 mm), while the distribution was relatively uniform (the average interval was 2 mm). The size and distribution of air pockets depended on the mixing uniformity of the vesicant and the cement powder. As for the influence by existence or absence of the microbeads on the micro structure, the distribution of gravels was relatively dense (the average interval was 4 mm), which was because more amount of gravels was added into S2 (Fig. 5(f)). In terms of S3, the gravels and the surrounding microbeads together formed phononic crystals (Fig. 5(g)), where the interval became slightly larger (the average spacing was 5 mm). Few of the air pockets could be found (their distribution density was obviously less than that in S1). In addition, in S7, due to the sinking of the gravels at the bottom of the sample (Fig. 5(h)), most of the microbeads and pores were squeezed to the upper side of the sample, whose distribution were relatively sparse here.

7. Sound absorption tests

The transfer function method is suitable for the research of the sound absorption and the comparison of the sound absorption performance of materials. It measures the sound absorption coefficient of specimens,

which is related to the orientation of sound wave incidence and installation conditions. Therefore, an impedance tube was generally applied to study the acoustic properties of materials independent of the sample size (Fig. 6(a)). During the test, the prepared specimen was loaded into a square plastic fixture, and a small amount of vacuum grease was applied to the lateral surfaces of the specimen to ensure that no gap remained between the specimen and fixture. The fixture was then installed in the impedance tube. The speaker was set to emit white noise with the frequency continuously increasing from 500 to 1900 Hz, which was determined by the measurement range of the impedance tube [36]. The sound pressures were measured by microphones (BSWA TECH MPA416-2) on both sides of the specimen, which could collect signals. Afterwards, the sound was transferred to voltage signals by the signal conditioner (SKC Q882) and measured by the data acquisition (DAQ) board (National Instrument USB-4431). In order to eliminate the influence of the reflection of sound wave from the other end of the tube on the measurement of sound absorption performance, a sponge was placed at the other end of the impedance tube to absorb this part of the sound wave. However, some periodic ripple patterns appeared in the sound absorption curves of all samples. This could be caused by standing waves reflected from the acoustic waves inside the tube. Although a sponge was placed at the end of the tube to absorb sound waves through the specimen, a small amount of sound waves could still reflect from the end. Therefore, it was necessary to remove that ripples so as to obtain more accurate absorption coefficients [37]. Finally, sound absorption coefficients were plotted against frequencies for the seven tested specimens, as shown in Fig. 6(b).

According to the results in Fig. 6(b), pure cement (S1) did not

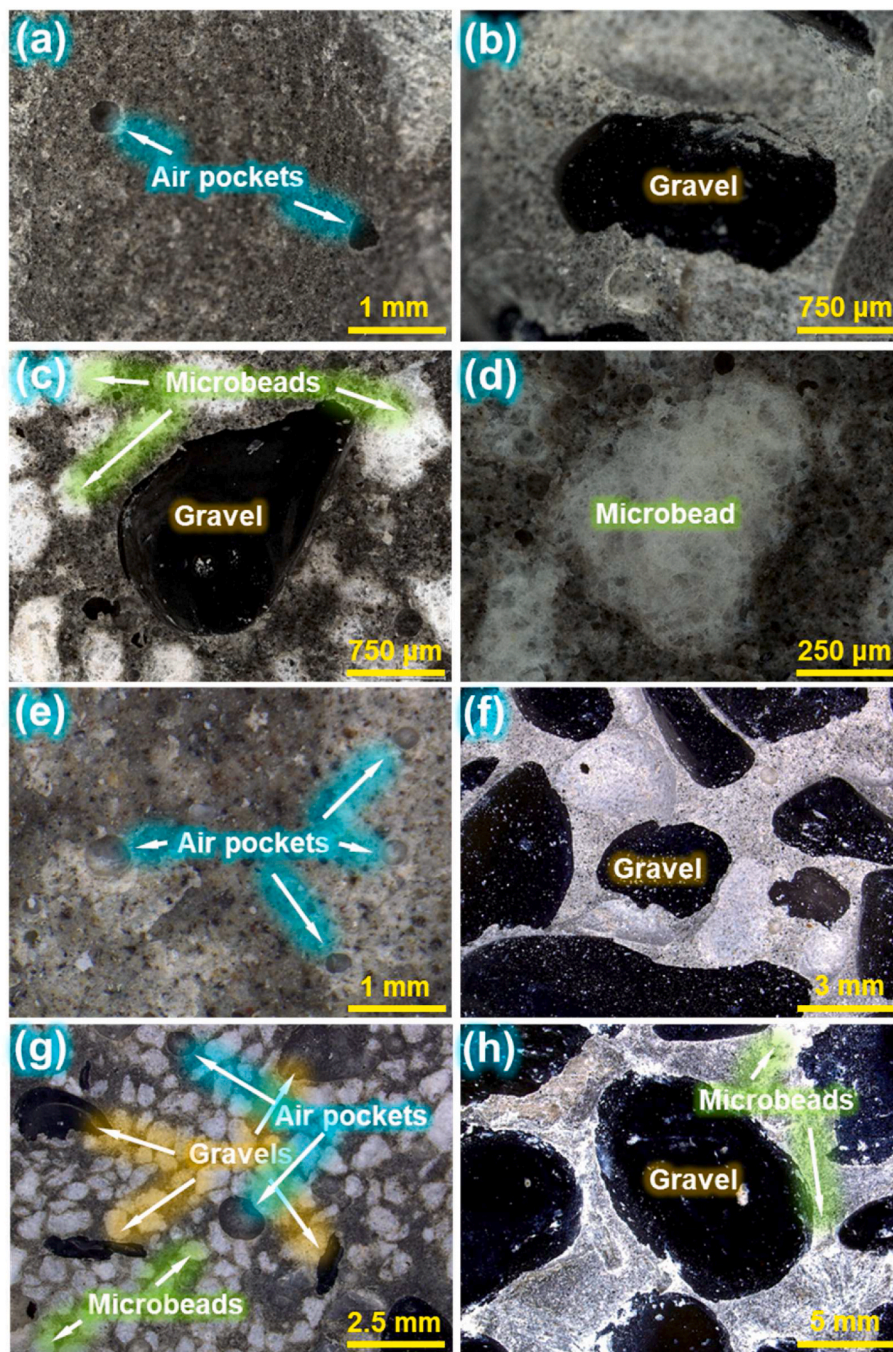


Fig. 5. Digital microscope images of the cement matrix sound-absorbing composite. (a) The microstructure near the air pockets in specimen S1; (b) the microstructure around a gravel particle in specimen S2; (c) the microstructure of a gravel particle and its surrounding microbeads in specimen S3; (d) the microstructure inside a microbead in specimen S3; (e) the air pockets distribution in S1; (f) the gravels distribution in S2; (g) the material distribution in S3; (h) the material distribution in S7.

provide a good sound absorption performance. In the low-frequency band (500–800 Hz), the sound absorption coefficient remained relatively stable. However, it obviously fluctuated in the medium- and high-frequency bands (larger than 800 Hz). This occurred because the addition of vesicant resulted in many pores in the concrete. They affected the propagation of sound waves within the specimen. However, the sound absorption coefficients of the concrete mixtures containing three types of gravel particles (specimens S2 through S7) was found to increase with increasing frequency to peak values, and then was found to decrease with further increasing frequency. In the specimen groups with the same gravel particle sizes, the sound absorption coefficients of specimens containing microbeads (specimens S3, S5, and S7) were higher. The 4-mm gravel samples (specimens S2 and S3) exhibited the highest sound absorption coefficient with a peak value at frequency of 1490 Hz. This

agrees with the numerical simulation results corresponding to the band gap frequency of the 5-mm element size, as shown in Fig. 4(b). The 6-mm gravel samples (specimens S4 and S5) exhibited the peak absorption coefficients, similar to those of the 4-mm gravel specimens, at frequency of 1020 Hz. This frequency was slightly higher than the band gap frequency determined by the numerical simulation with the 7.5-mm element size, as shown in Fig. 4(b). This may be due to the difference in material properties between the numerical simulations and the experiments. The peak absorption coefficient of the 8-mm gravel samples (specimen S6 and S7) occurred at frequency of 810 Hz, which was consistent with the numerical simulation results corresponding to the band gap frequency of the 10-mm element size, as shown in Fig. 4(b). Nevertheless, the sound absorption performances of these two specimens (S6 and S7) were relatively poor compared to the other specimens,

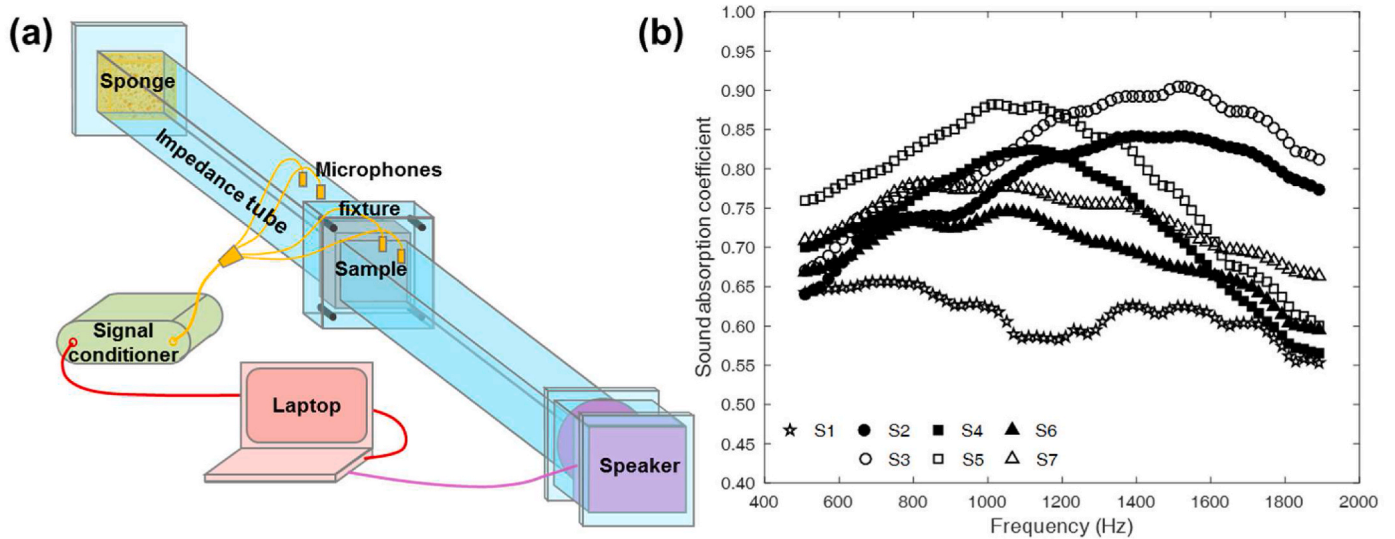


Fig. 6. The methodology and results of the physical validation. (a) The setup of the measurement system; (b) sound absorption performance of the concrete with different mixture proportions.

which may be due to the rapid precipitation of large-size gravel particles in the moulding process. This resulted in an uneven material distribution. In conclusion, the gravel particle size affects the sound absorption performance of concrete at the different frequencies. The addition of microbeads obviously enhances the sound absorption ability. The reason is that a large number of connected pores occurs in the microbeads. Hence, water saturates the microbeads during concrete preparation. Therefore, a large amount of air is transferred from the microbeads to the cement to improve the sound absorption performance of the concrete. Even for the same size of gravels, the distribution density of gravels in two samples (such as S2 and S3) with or without microbeads was different (as shown in Fig. 5 (f, g)). Comparing the absorption coefficient curves of S1 and S2, it could be seen that the addition of gravels significantly improved the sound absorption performance. This was because gravels could refract and reflect sound waves, which weakened the energy of sound waves more than that in plain cement. However, the effect was not as obvious as that of phononic crystals composed of gravels and microbeads (S3). On the other hand, the sound absorption performance of large and scattered gravels (S7) was not as good as that of small and concentrated gravels (S3). The reason was that the over dispersed gravels made most part of the sample be similar to a single medium such as plain cement, which greatly reduced the possibility of refraction and reflection of sound waves at the interface between the gravels and microbeads.

8. Conclusions

This study was designed to investigating the sound absorption performance of phononic crystal consisted of cement embedded by gravels and microbeads, where the theoretical derivation, numerical simulation and physical validation were implemented successively. Based on the obtained results, the main conclusions can be drawn from this study as follows:

- (1) The sound absorption capability of cementitious composites made by cement embedded by gravels and microbeads could be improved via band gap maximization. With the smoothed boundary representation, the band gap was successfully expanded. The results indicated that solid volume fraction $V = 0.5$ was the best value for band gap maximization purposes, accompanied by a round shape.

- (2) The images from digital microscope revealed that the microbeads could weaken the adhesion between the gravel particles and cement. It could also provide more pores, which together with the cement-based material produced a lower-density mixture consisting of phononic crystals. On the other hand, large gravel particles might product an uneven material distribution. Therefore, it is very important to select the appropriate gravel size.
- (3) According to the physical validations, the microbeads could significantly improve the sound absorption performance. The maximum sound absorption coefficient of the phononic crystal composed of 4 mm gravels and surrounding microbeads can reach 90%. The frequency corresponding to the peak value is 1490 Hz, which is consistent with the frequency range of the band gap from the theoretical derivation and simulation analysis.

There are also some defects in the experiment. For example, the range of the impedance tube used in the experiment was only 400–2000 Hz, which could not test the sound absorption effect of lower or higher frequency. In the future research, samples with other sizes can be made to match other impedance with different measuring range. In that case, the sound absorption effect of a wider frequency can be tested. Still, the methodology of designing and optimizing this phononic crystal is innovative and expected to be applied to the design of cementitious structures to achieve sound-proof structures.

CRediT authorship contribution statement

Sen Lin: Project administration, Funding acquisition, Supervision, Methodology, Conceptualization, Formal analysis. **Genbao Zhang:** Funding acquisition, Conceptualization, Data curation, Visualization, Writing -original draft. **Junbo Sun:** Conceptualization, Methodology, Data curation. **Shilin He:** Methodology, Investigation. **Changfu Chen:** Conceptualization, Data curation, Visualization. **Amr M. Morsy:** Data curation, Visualization, Writing - review & editing. **Xiangyu Wang:** Methodology, Conceptualization.

Declaration of competing interest

The authors declare that they have no known competing financial interests or personal relationships that could have appeared to influence the work reported in this paper.

Acknowledgements

The authors gratefully acknowledge the financial support provided by the Systematic Project of the Guangxi Key Laboratory of Disaster Prevention and Structural Safety (grant number 2019ZDK011), the

National Natural Science Foundation of China (grant numbers 11802082, 51908201), the Natural Science Foundation of Hunan Province (grant numbers 2020JJ5027, 2020JJ5024) and the State Key Laboratory of Advanced Design and Manufacturing for Vehicle Body (grant numbers 51965009).

Appendix

The governing equations of wave propagation are:

$$\rho u_{p,tt} = \sigma_{pq,q}$$

$$\sigma_{pq} = C_{pqrs} \varepsilon_{rs}$$

where u_p is the displacement, σ_{pq} is the stress, ε_{rs} is the strain and C_{pqrs} is the stiffness tensor.

According to the Bloch theory, the displacement vector can be expressed as:

$$\mathbf{u}_{(\mathbf{r},\mathbf{k})} = \mathbf{u}_{(\mathbf{r})} e^{i(\mathbf{k}\cdot\mathbf{r})} e^{i\omega t}$$

where:

$$\mathbf{u}_{(\mathbf{r})} = [u_{x1}, u_{y1}, u_{z1}, \dots, u_{x8}, u_{y8}, u_{z8}]^T$$

The discretized material law and the kinematic relations are given for one element as follows:

$$\varepsilon_{6 \times 1} = L_{6 \times 3} \cdot \mathbf{u}_{(\mathbf{r},\mathbf{k})_{3 \times 1}}$$

where the elastic strain operator matrix L is given as:

$$L = \frac{\partial}{\partial x} L_1 + \frac{\partial}{\partial y} L_2 + \frac{\partial}{\partial z} L_3 = \frac{\partial}{\partial x} \begin{bmatrix} 1 & 0 & 0 \\ 0 & 0 & 0 \\ 0 & 0 & 0 \\ 0 & 1 & 0 \\ 0 & 0 & 0 \\ 0 & 0 & 1 \end{bmatrix} + \frac{\partial}{\partial y} \begin{bmatrix} 0 & 0 & 0 \\ 0 & 1 & 0 \\ 0 & 0 & 0 \\ 1 & 0 & 0 \\ 0 & 0 & 1 \\ 0 & 0 & 0 \end{bmatrix} + \frac{\partial}{\partial z} \begin{bmatrix} 0 & 0 & 0 \\ 0 & 0 & 0 \\ 0 & 0 & 1 \\ 0 & 1 & 0 \\ 0 & 1 & 0 \\ 1 & 0 & 0 \end{bmatrix}$$

The quadratic approximation function $N_i(x,y,z)$ is calculated in the local coordinate system as:

$$\mathbf{u}_{(\mathbf{r},\mathbf{k})_{3 \times 1}} = N_{3 \times 24} \cdot \check{\mathbf{u}}_{(\mathbf{r},\mathbf{k})_{24 \times 1}}$$

where $\check{\mathbf{u}}$ is the local displacement and N is the shape function matrix.

$$\begin{aligned} \varepsilon &= \left[\left(L_1 \frac{\partial N}{\partial x} + L_2 \frac{\partial N}{\partial y} + L_3 \frac{\partial N}{\partial z} \right) + (L_1 N i k_x + L_2 N i k_y + L_3 N i k_z) \right] e^{i(\mathbf{k}\cdot\mathbf{r})} e^{i\omega t} \check{\mathbf{u}}(\mathbf{r}) \\ &= (B_1 + B_2 i k_x + B_3 i k_y + B_4 i k_z) e^{i(\mathbf{k}\cdot\mathbf{r})} e^{i\omega t} \check{\mathbf{u}}(\mathbf{r}) = B \check{\mathbf{u}}_{(\mathbf{r},\mathbf{k})} \end{aligned}$$

where:

$$B = B_1 + B_2 i k_x + B_3 i k_y + B_4 i k_z$$

$$B_1 = L_1 \frac{\partial N}{\partial x} + L_2 \frac{\partial N}{\partial y} + L_3 \frac{\partial N}{\partial z}, \quad B_2 = L_1 N, \quad B_3 = L_2 N, \quad B_4 = L_3 N$$

Derivate \mathbf{u} about t is obtained as:

$$\dot{\mathbf{u}}_{(\mathbf{r},\mathbf{k})} = \mathbf{u}_{(\mathbf{r},\mathbf{k})} i\omega$$

The Lagrangian L_a for one element is:

$$\begin{aligned} L_a &= \frac{1}{2} \int_t \int_h \int_A \left(\rho \dot{\mathbf{u}}_{(\mathbf{r},\mathbf{k})}^T \dot{\mathbf{u}}_{(\mathbf{r},\mathbf{k})} - \varepsilon^T C \varepsilon \right) dAdhdt \\ &= \frac{1}{2} \int_t \left(\omega^2 \check{\mathbf{u}}_{(\mathbf{r},\mathbf{k})}^T m_e \check{\mathbf{u}}_{(\mathbf{r},\mathbf{k})} - \check{\mathbf{u}}_{(\mathbf{r},\mathbf{k})}^T k_e \check{\mathbf{u}}_{(\mathbf{r},\mathbf{k})} \right) dt \end{aligned}$$

where m_e and k_e are the stiffness and mass matrices, respectively, for one element.

$$\begin{aligned}
k_e^i &= \int_h \int_A B^T C B dA dh \\
&= \int_h \int_A (B_1^T - B_2^T i k_x - B_3^T i k_y - B_4^T i k_z) C (B_1 + B_2 i k_x + B_3 i k_y + B_4 i k_z) dA dh \\
&= \int_h \int_A k_1^i + k_2^i i k_x + k_3^i i k_y + k_4^i i k_z + k_5^i k_x^2 + k_6^i k_y^2 + k_7^i k_z^2 + k_8^i k_x k_y + k_9^i k_x k_z + k_{10}^i k_y k_z dA dh
\end{aligned}$$

where:

$$k_1^i = B_1^T C B_1$$

$$k_2^i = B_1^T C B_2 - B_2^T C B_1$$

$$k_3^i = B_1^T C B_3 - B_3^T C B_1$$

$$k_4^i = B_1^T C B_4 - B_4^T C B_1$$

$$k_5^i = B_2^T C B_2$$

$$k_6^i = B_3^T C B_3$$

$$k_7^i = B_4^T C B_4$$

$$k_8^i = B_2^T C B_3 + B_3^T C B_2$$

$$k_9^i = B_2^T C B_4 + B_4^T C B_2$$

$$k_{10}^i = B_3^T C B_4 + B_4^T C B_3$$

References

- [1] S. Yang, et al., Focusing of sound in a 3D phononic crystal, *Phys. Rev. Lett.* 93 (2) (2004), 024301.
- [2] S. Lin, et al., Shell buckling: from morphogenesis of soft matter to prospective applications, *Bioinspiration Biomimetics* 13 (5) (2018), 051001.
- [3] R.H. Olsson III, I. El-Kady, Microfabricated phononic crystal devices and applications, *Meas. Sci. Technol.* 20 (1) (2008), 012002.
- [4] O. Sigmund, J.S. Jensen, Systematic design of phononic band-gap materials and structures by topology optimization, *Phil. Trans. Roy. Soc. Lond.* 361 (1806) (2003) 1001–1019.
- [5] L. Shi, et al., Spectral element method for band-structure calculations of 3D phononic crystals, *J. Phys. Appl. Phys.* 49 (2016) 455102.
- [6] P.-F. Hsieh, T.-T. Wu, J.-H. Sun, Three-dimensional phononic band gap calculations using the FDTD method and a PC cluster system, *IEEE Trans. Ultrason. Ferroelectrics Freq. Contr.* 53 (1) (2006) 148–158.
- [7] G.A. Gazonas, et al., Genetic algorithm optimization of phononic bandgap structures, *Int. J. Solid Struct.* 43 (18) (2006) 5851–5866.
- [8] Z.-f. Liu, B. Wu, C.-f. He, Band-gap optimization of two-dimensional phononic crystals based on genetic algorithm and FPWE, *Waves Random Complex Media* 24 (3) (2014) 286–305.
- [9] M.P. Bendsoe, O. Sigmund, *Topology Optimization: Theory, Methods, and Applications*, Springer Science & Business Media, 2013.
- [10] S. Lin, et al., On the interaction of biological and mechanical factors in leaf vein formation, *Adv. Eng. Software* 149 (2020) 102905.
- [11] M.Y. Wang, X. Wang, D. Guo, A level set method for structural topology optimization, *Comput. Methods Appl. Mech. Eng.* 192 (1) (2003) 227–246.
- [12] X. Huang, Y. Xie, Convergent and mesh-independent solutions for the bi-directional evolutionary structural optimization method, *Finite Elem. Anal. Des.* 43 (14) (2007) 1039–1049.
- [13] X. Huang, Y. Xie, Bi-directional evolutionary topology optimization of continuum structures with one or multiple materials, *Comput. Mech.* 43 (3) (2009) 393–401.
- [14] D. Da, et al., Evolutionary topology optimization of continuum structures with smooth boundary representation, in: *Structural and Multidisciplinary Optimization*, 2017.
- [15] K. Su, Q. Wei, X. Zhang, Tunable and augmented plasmon resonances of Au/ Si O 2/ Au nanodisks, *Appl. Phys. Lett.* 88 (6) (2006), 063118.
- [16] A. Khelif, et al., Complete band gaps in two-dimensional phononic crystal slabs, *Phys. Rev.* 74 (2006), 046610.
- [17] T.-T. Wu, L.-C. Wu, Z.-G. Huang, Frequency band-gap measurement of two-dimensional air/silicon phononic crystals using layered slanted finger interdigital transducers, *J. Appl. Phys.* 97 (9) (2005), 094916.
- [18] S. Benchabane, et al., Evidence for complete surface wave band gap in a piezoelectric phononic crystal, *Phys. Rev.* 73 (6) (2006), 065601.
- [19] R. Sainidou, N. Stefanou, A. Modinos, Formation of absolute frequency gaps in three-dimensional solid phononic crystals, *Phys. Rev. B* 66 (21) (2002) 212301.
- [20] Z. Liu, C.T. Chan, P. Sheng, Three-component elastic wave band-gap material, *Phys. Rev. B* 65 (16) (2002) 165116.
- [21] J. Sun, et al., Prediction of permeability and unconfined compressive strength of pervious concrete using evolved support vector regression, *Construct. Build. Mater.* 207 (2019) 440–449.
- [22] G. Ma, et al., Electromagnetic and microwave absorbing properties of cementitious composite for 3D printing containing waste copper solids, *Cement Concr. Compos.* 94 (2018), 453–461.
- [23] P.-H. Chen, C. Xu, D.D.L. Chung, Sound absorption enhancement using solid–solid interfaces in a non-porous cement-based structural material, *Compos. B Eng.* 95 (2016) 453–461.
- [24] C. Arenas, et al., Technical specifications for highway noise barriers made of coal bottom ash-based sound absorbing concrete, *Construct. Build. Mater.* 95 (2015) 585–591.
- [25] M. Vašina, et al., The acoustical properties of consolidated expanded clay granulates, *Appl. Acoust.* 67 (8) (2006) 787–796.
- [26] S.B. Park, D.S. Seo, J. Lee, Studies on the sound absorption characteristics of porous concrete based on the content of recycled aggregate and target void ratio, *Cement Concr. Res.* 35 (9) (2005) 1846–1854.
- [27] V. Tiwari, A. Shukla, A. Bose, Acoustic properties of cenosphere reinforced cement and asphalt concrete, *Appl. Acoust.* 65 (3) (2004) 263–275.
- [28] H. Kim, J. Hong, S. Pyo, Acoustic characteristics of sound absorbable high performance concrete, *Appl. Acoust.* 138 (2018) 171–178.

- [29] J. Amirian, et al., Incorporation of alginate-hyaluronic acid microbeads in injectable calcium phosphate cement for improved bone regeneration, *Mater. Lett.* 272 (2020) 127830.
- [30] H.-W. Dong, et al., Topological optimization of two-dimensional phononic crystals based on the finite element method and genetic algorithm, *Struct. Multidiscip. Optim.* 50 (4) (2014) 593–604.
- [31] R. Ramírez, M.C. Böhm, Simple geometric generation of special points in brillouin-zone integrations, *Two-dimens. Bravais Lattices* 30 (3) (2010) 391–411.
- [32] J. Vasseur, et al., Complete acoustic band gaps in periodic fibre reinforced composite materials: the carbon/epoxy composite and some metallic systems, *J. Phys. Condens. Matter* 6 (42) (1994) 8759.
- [33] X. Huang, Z. Zuo, Y. Xie, Evolutionary topological optimization of vibrating continuum structures for natural frequencies, *Comput. Struct.* 88 (5) (2010) 357–364.
- [34] Y.F. Li, X. Huang, S. Zhou, Topological design of cellular phononic band gap crystals, *Materials* 9 (3) (2016) 186.
- [35] D. Cuiyun, et al., Sound absorption characteristics of a high-temperature sintering porous ceramic material, *Appl. Acoust.* 73 (9) (2012) 865–871.
- [36] X.F. Fu, et al., A 3D space coiling metamaterial with isotropic negative acoustic properties, *Appl. Phys. Lett.* 111 (25) (2017) 251904.
- [37] S. Lawanwadeekul, et al., Applying the ensemble averaging method with a pressure-velocity sensor to measure sound absorption characteristics of porous clay bricks, *Appl. Acoust.* 164 (2020) 107250.